*Chinese Journal of*
**POLYMER SCIENCE**

RESEARCH ARTICLE

https://doi.org/10.1007/s10118-026-3717-3
*Chinese J. Polym. Sci.* **2026**, *44*, 3476–3489

# Synergistically Enhanced Time-resolved Dual-mode Emission in Flexible Poly(vinyl alcohol) Films for Dynamic Information Encryption

Xiao-Ya Liu[a], Jin-Fang Liu[a], Ahmed Olalekan Omoniyi[a,b], and Jian-Fu Zhang[a*]

[a] *Jilin Provincial Science and Technology Innovation Centre of Optical Materials and Chemistry, School of Chemistry and Environmental Engineering, Changchun University of Science and Technology, Changchun 130022, China*
[b] *Zhongshan Institute of Changchun University of Science and Technology, Zhongshan 528437, China*

Electronic Supplementary Information

**Abstract** Long-lived room-temperature phosphorescent (RTP) films are attractive for information encryption, yet binary host-guest polymer systems often suffer from weak afterglow and limited operational reliability. In this study, we developed a ternary RTP system using poly(vinyl alcohol) (PVA) as the host matrix, coumarin derivatives as the emissive guests, and a third component, boric acids (BA/3-BBA), tannic acid (TA), or metal salts ($Ca^{2+}$, $Mn^{2+}$, $Zn^{2+}$), to regulate triplet-state generation and stabilization. Structural analysis confirmed the guest incorporation and borate network formation. Guest loading decreased the visible transmittance, whereas borate crosslinking partially restored the transparency and improved the thermal integrity (main decomposition near 430 °C). The films exhibit good mechanical performance (for PVA-A: 32.70 MPa tensile strength; 245.60 MPa modulus; and 63.82 MJ·m$^{-3}$ toughness), while crosslinking/coordination increases stiffness (up to 1479.55 MPa modulus for PVA-A-TA). The introduction of the third component enhanced the RTP and photoluminescence quantum yield (PLQY), except for $Mn^{2+}$, which induced quenching. The materials also demonstrated reversible moisture response and good UV stability. Leveraging time-gated afterglow, multi-level information encryption is achieved using dynamic digit displays and an ASCII matrix with decoy and delayed outputs. This ternary strategy enables the practical optimization of PVA-based flexible RTP materials for high-security anti-counterfeiting and information encryption applications.

**Keywords** Room-temperature phosphorescence (RTP); Poly(vinyl alcohol) (PVA); Coumarin derivatives; Host-guest system; Information encryption

**Citation:** Liu, X. Y.; Liu, J. F.; Omoniyi, A. O.; Zhang, J. F. Synergistically enhanced time-resolved dual-mode emission in flexible poly(vinyl alcohol) films for dynamic information encryption. *Chinese J. Polym. Sci.* **2026**, *44*, 3476–3489.

## INTRODUCTION

Information security technologies underpin the modern digital society by protecting the integrity and authenticity of data during storage, transmission, and exchange.[1,2] Beyond cryptographic algorithms, physical information encryption—encoding information into materials that are difficult to replicate and can be authenticated through controlled readout—has become increasingly important for anti-tampering and brand protection. Luminescent materials are particularly attractive for this purpose because they enable contactless excitation and readout, high spatial resolution patterning, and compatibility with scalable fabrication processes, such as coating, printing, and film casting.[3] However, most fluorescence-based security features provide only instantaneous signals that are easily detected and reproduced, and their readout is often compromised by background fluorescence, scattering, and ambient light interference.[4] These limitations motivate the design of security materials whose optical signatures can be decoded in a time-dependent manner.

Organic room-temperature phosphorescence (RTP) materials[5] provide a compelling platform for time-gated encryption and dynamic anti-counterfeiting.[6–10] In contrast to fluorescence, RTP arises from long-lived triplet excitons and can be selectively collected after the excitation source is removed, offering high signal-to-noise ratio and strong resistance to optical interference.[11–13] The temporal dimension of phosphorescence enables multi-level authentication, where information can appear, transform, or disappear over time rather than remaining static. Despite these advantages, practical organic RTP systems remain difficult to realize because triplet excitons are inherently vulnerable to non-radiative relaxation and quenching by oxygen and moisture. Consequently, many RTP materials exhibit insufficient afterglow intensity, short lifetime, and poor environmental stability[14,15] which limits the reliability of real-world encryption scenarios involving repeated handling and exposure to ambient conditions.

Accordingly, strategies to enhance organic RTP typically

* Corresponding author, E-mail: zhangjianfu@cust.edu.cn
Received February 20, 2026; Accepted April 16, 2026; Published online July 1, 2026

address two fundamental requirements: one, increasing triplet exciton populations by promoting intersystem crossing (ISC), and second, suppressing non-radiative deactivation of triplet states by restricting molecular motion and minimizing quenching pathways.[16–21] On the one hand, ISC can be enhanced by introducing carbonyl-rich chromophores, strengthening the charge-transfer character, or incorporating metal-assisted spin-orbit coupling to open efficient singlet-to-triplet transition channels.[22] On the other hand, non-radiative decay and oxygen quenching can be suppressed by constructing rigid microenvironments *via* crystallization, host-guest confinement, supramolecular assembly, or polymer encapsulation, which immobilize luminophores and hinder oxygen diffusion.[23–25] Prior studies have demonstrated that hydrogen-bonding networks in polymer matrices can activate long-lived phosphorescence, and that auxiliary metal ions can further improve RTP by coordination-induced rigidification together with coordination-assisted enhancement of spin–orbit coupling and ISC.[26] These advances indicate that combining electronic state regulation with structural confinement is an effective pathway for higher-performance RTP.

Nevertheless, a practical gap persists between many reported RTP systems and the stringent requirements for time-gated security materials. A high RTP performance is often achieved in rigid crystalline solids or strongly crosslinked matrices that are difficult to process, pattern, or integrate into flexible devices.[27] Meanwhile, mechanically compliant RTP films may still suffer from weak afterglow brightness, rapid degradation under humidity, or trade-offs, in which increasing rigidity undermines flexibility and durability. Polymer matrices[28–34] are promising for closing this gap because they offer a tunable microenvironment for photophysical regulation, along with scalable manufacturability. Among them, poly(vinyl alcohol) (PVA) is attractive because of its high density of hydroxyl (—OH) groups,[35–38] which enable extensive intermolecular interactions and network formation that can immobilize chromophores, suppress vibrational relaxation, and hinder oxygen diffusion. However, the abundant —OH groups also promote moisture uptake; water-induced plasticization can soften PVA, reduce mechanical strength, and attenuate phosphorescence. Achieving strong RTP while simultaneously improving flexibility and environmental stability remains a key challenge for PVA-based security films.

Herein, we address this challenge by developing a synergistically enhanced time-gated dual-mode emission in flexible PVA films through a third-component modulation strategy. Our design began with a binary PVA/coumarin derivative (PVA-G; G = guest). The coumarin core is a donor-$\pi$-acceptor-conjugated framework that can form an intermolecular charge-transfer (ICT) state, the strong ICT character favors spin-orbit coupling and facilitates ISC when the chromophore is appropriately confined. In the PVA matrix, hydrogen bonding between PVA —OH groups and the carbonyl/amino functionalities of coumarin helps to immobilize the luminophore and suppress non-radiative decay; however, the binary PVA-G system alone remains limited in afterglow intensity and stability for demanding encryption applications. Therefore, we introduce a third component to create complementary interactions that simultaneously enhance the ISC and triplet population, suppress non-radiative transitions and environmental quenching, and improve mechanical robustness. Specifically, boric acid (BA) and biphenyl-3-boronic acid (3-BBA) form B—O—C linkages with PVA to generate a denser covalent-hydrogen-bond hybrid network with improved resistance to moisture and strengthened triplet confinement; tannic acid (TA), which is rich in phenolic hydroxyl groups, forms multi-point hydrogen bonds with PVA that increases crosslink density, consumes free —OH groups to reduce water absorption, and scavenges reactive oxygen species to mitigate oxygen-related quenching; and metal ions ($Ca^{2+}$, $Mn^{2+}$, $Zn^{2+}$) coordinate with coumarin carbonyl groups to lock chromophores into rigid micro-domains, suppress thermal relaxation, and promote coordination-assisted spin-orbit coupling and ISC. By integrating covalent crosslinking, hydrogen-bond reinforcement, and metal coordination within the PVA-G platform, we established a generalizable strategy for designing flexible RTP films that support time-gated readout—instant fluorescence under excitation, followed by delayed phosphorescence afterglow for dynamic encryption and anti-counterfeiting.

## EXPERIMENTAL

### Materials

PVA (alcoholysis degree: 99%, polymerization degree: 1700) and PVA (alcoholysis degree: 99%, polymerization degree: 2400) were purchased from Anhui Wanwei Group Co., Ltd. 7-Amino-4-methylcoumarin (G-A), 7-diethylaminocoumarin-3-carboxylic acid (G-C) was purchased from Leyan Reagents. 6,7-Dihydroxycoumarin (G-B), boric acid, 3-biphenylboronic acid, and tannic acid were purchased from Ron's Reagent. Anhydrous zinc chloride was purchased from the Beijing Chemical Plant. Anhydrous calcium chloride, zinc sulfate, and manganese chloride were obtained from Tianjin Xintong Fine Chemical Co., Ltd. Anhydrous ethanol was purchased from National Pharmaceutical Group Chemical Reagent Co., Ltd. Deionized water was used as the dispersed phase, and all reagents were analytically pure without further purification before use.

### Preparation of PVA-G Films

The preparation of a PVA-7-amino-4-methylcoumarin (PVA-A) film is described as a representative example. Unless otherwise specified, all PVA-G films were prepared using 1799PVA (alcoholysis degree 99%, polymerization degree is about 1700). PVA (1.2 g) was dissolved in deionized water (24 mL) and stirred at 90 °C for 1 h to obtain a homogeneous PVA solution with a concentration of 50 mg/mL. A G-A ethanol solution (5 mg/mL) was prepared by dissolving G-A (40 mg) in anhydrous ethanol (8 mL). The two solutions were mixed and subjected to ultrasonic treatment for 1 h to ensure a uniform dispersion. The resulting solution was cast onto a 2.0 cm × 2.0 cm quartz plate, followed by solvent evaporation in a vacuum oven at 60 °C, yielding a transparent film. Films with different G-A doping concentrations were prepared using the same procedure, with only the amount of G-A adjusted. The G-A concentration gradients used in this study were 20, 30, 40, 50, and 60 mg per 8 mL of ethanol. The preparation methods for the PVA-B and PVA-C films were identical to those for the PVA-A film. For comparison, 2499PVA (alcoholysis degree 99%, polymerization degree is about 2400)

https://doi.org/10.1007/s10118-026-3717-3

was used following the same procedure.

### Preparation of PVA-A-crosslinking Agent Films

The preparation of a PVA-A-boric acid (PVA-A-BA) film is described as an example. PVA (1.2 g) was dissolved in deionized water (24 mL) and stirred at 90 °C for 1 h to obtain a PVA solution (50 mg/mL). G-A ethanol solution (5 mg/mL) was prepared by dissolving G-A (40 mg) in anhydrous ethanol (8 mL). BA (30 mg) was dissolved in an appropriate amount of deionized water to obtain a clear BA solution. PVA, G-A, and BA solutions were mixed and ultrasonicated for 1 h. The mixture was then cast onto a 2.0 cm × 2.0 cm quartz substrate and dried in a vacuum oven at 60 °C to form a transparent film. Films with different BA contents were prepared following the same procedure, with BA concentrations of 10, 30, 50, and 70 mg per 2 mL of deionized water. The preparation methods for the PVA-A-tannic acid (PVA-A-TA) and PVA-A-biphenyl-3-boronic acid (PVA-A-3-BBA) films were identical to those for the PVA-A-BA film.

### Preparation of PVA-A-$M^{2+}$ Film

The preparation of the PVA-A-$CaCl_2$ film is described as an example. PVA (1.2 g) was dissolved in deionized water (24 mL) and stirred at 90 °C for 1 h to obtain a PVA solution (50 mg/mL). G-A ethanol solution (5 mg/mL) was prepared by dissolving G-A (50 mg) in anhydrous ethanol (8 mL). $CaCl_2$ (20 mg) was dissolved in deionized water (2 mL) to form a $CaCl_2$ solution. The three solutions were mixed, ultrasonicated for 1 h, and then cast onto a 2.0 cm × 2.0 cm quartz substrate. A transparent film was obtained after drying in a vacuum oven at 60 °C. The preparation methods for the PVA-A-$MnCl_2$, PVA-A-$ZnCl_2$, and PVA-A-$ZnSO_4$ films were identical to those for the PVA-A-$CaCl_2$ film.

### Characterizations

Fourier transform infrared (FTIR) spectra were recorded using a Shimadzu FTIR-8400S spectrometer to analyze the chemical structures of the samples. The UV-visible transmission spectra were measured using a UV-Vis spectrophotometer (UV-2600, Shimadzu, Japan). Steady-state photoluminescence (PL) and delayed emission spectra were recorded using an FL-7100 fluorescence spectrometer under ambient conditions. The photoluminescence quantum yield (PLQY) of all the films was measured using an FLS980 spectrometer (Edinburgh Instruments) equipped with an integrating sphere under ambient conditions. Phosphorescence lifetimes were measured using an Edinburgh FLS1000 fluorescence spectrometer. The mechanical properties were evaluated *via* stress-strain measurements using an electronic universal testing machine (PT14-014, 20 kN, China). Thermal stability was analyzed by thermogravimetric analysis (TGA) using a Mettler TGA2 instrument under a nitrogen atmosphere at a heating rate of 10 °C/min. Ultrasonic treatment was performed using an ultrasonic cleaner (JP-010; Jiemeng, Shenzhen Jiemeng Cleaning Equipment Co., Ltd., China).

## RESULTS AND DISCUSSION

### Design Rationale and Photophysical Mechanism of the PVA-G Platform

Flexible RTP platforms were constructed using PVA as the polymer host and coumarin derivatives as luminescent organic guests while introducing a third component to regulate the microstructure and excited-state dynamics (Fig. 1). PVA provides a dense —OH-rich network that (i) offers a rigid microenviron-

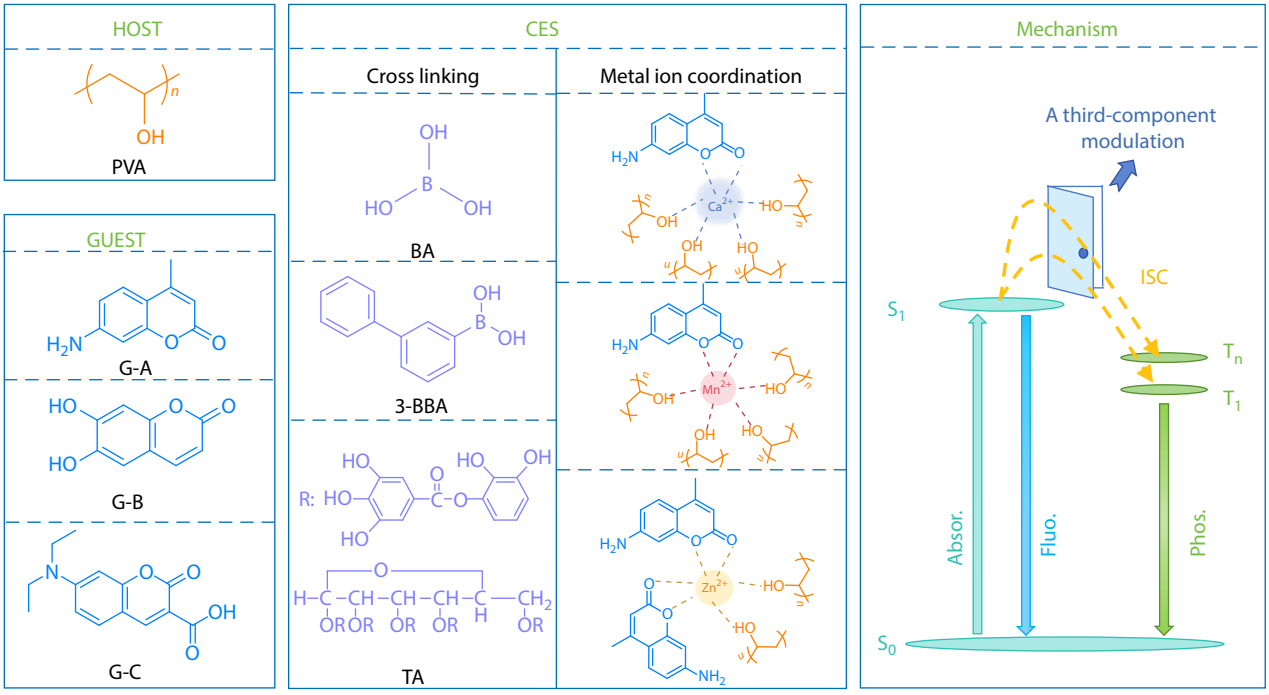


**Fig. 1** Molecular structures and proposed mechanism for the ternary PVA-G RTP system. The design consists of PVA as the host matrix, coumarin derivatives as organic guests, and a third component (crosslinkers or metal ions). Crosslinkers (BA, 3-BBA, TA) and metal ions (*e.g.*, $Ca^{2+}$, $Mn^{2+}$, $Zn^{2+}$) enhance triplet emission through a collaborative enhancement strategy (CES) by immobilizing the guest molecules through covalent bonding, hydrogen bonding, and/or coordination-induced rigidification, thereby suppressing non-radiative decay and enabling room-temperature phosphorescence after UV removal.

ment to suppress non-radiative deactivation, and (ii) supplies abundant interaction sites (hydrogen bonding and/or coordination) for guest immobilization. Three coumarin guests were employed: 7-amino-4-methylcoumarin (G-A), 6,7-dihydroxycoumarin (G-B), and 7-diethylaminocoumarin-3-carboxylic acid (G-C), whose amino/hydroxyl/carboxyl functionalities enable strong host–guest interactions and, crucially, provide specific binding sites for the third component. The third component was selected from two functional categories: (i) network-forming crosslinkers (boric acid, BA; biphenyl-3-boronic acid, 3-BBA; tannic acid, TA), and (ii) metal ions ($Ca^{2+}$, $Mn^{2+}$, $Zn^{2+}$ introduced as common salts). Although these additives operate through different chemical pathways, they share the same physical objectives: to immobilize the coumarin chromophores and reduce triplet-state losses by restricting molecular vibration/rotation and limiting the access of quenchers[39,40] (especially $O_2$ and moisture) to the emitting sites. Under excitation, coumarin molecules populate the singlet excited state ($S_1$) and emit a prompt blue fluorescence. A fraction of the excited states undergoes ISC to triplet manifolds ($T_n/T_1$); the rigidified PVA microenvironment suppresses non-radiative decay channels and enables delayed green RTP afterglow after the excitation is removed. In metal-ion-containing systems, coordination can additionally enhance ISC by increasing effective spin-orbit coupling *via* metal-ligand interactions.[41,42] This coordination-assisted ISC is expected to contribute to rigidification and metal-influenced spin-orbit coupling, both of which can increase triplet formation and stabilize triplet emission.

## Structural and Physical Properties of the PVA Composites

Fourier transform infrared (FTIR) spectroscopy confirmed the successful incorporation of coumarin guests into the PVA matrix, and subsequent network construction occurred without eliminating the characteristic PVA framework. As shown in Fig. 2(a), neat PVA exhibited a broad O—H stretching band in the 3337 $cm^{-1}$ region and a strong C—O stretching band in the 1084 $cm^{-1}$ region, consistent with its polyol-rich backbone. After the incorporation of the coumarin derivative, the modified films (PVA-A, PVA-B, and PVA-C) exhibited a distinct absorption near 1684 $cm^{-1}$, assignable to the lactone C=O stretching vi-

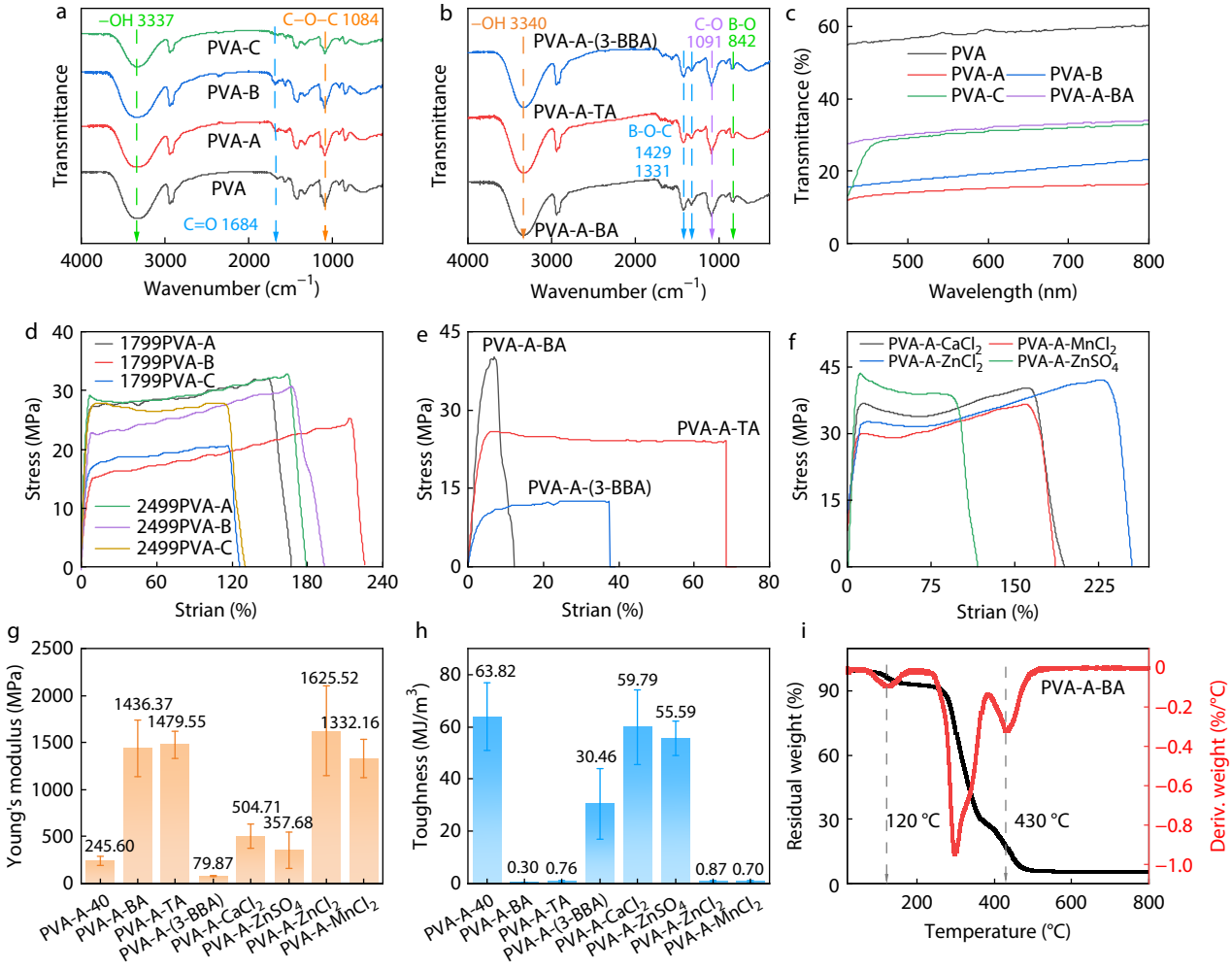


**Fig. 2** Structural and physical properties of PVA-G composite films. (a) FTIR spectra of PVA-G films; (b) FTIR spectra of PVA-G-A films modified with different crosslinkers (BA, TA, and 3-BBA); (c) UV-Vis transmission spectra of PVA-G composite films; (d) Stress-strain curves of PVA-G films; (e) Stress-strain curves of PVA-A-crosslinker films; (f) Stress-strain curves of PVA-A-$M^{2+}$ films; (g) Young's modulus and (h) toughness of PVA composite films; (i) TGA and DTG curves of PVA-A-BA film.

bration of coumarin, confirming the presence of the guest within the polymer film.[43] Importantly, the major PVA bands remained clearly detectable, indicating that the film-forming process and guest loading preserved the primary chemical identity of the polymer. In parallel, subtle changes in the —OH band shape and intensity are consistent with the altered hydrogen-bonding environments upon guest introduction, as expected for aromatic carbonyl-containing molecules embedded in a hydroxyl-rich matrix.[44] For the boron-based crosslinking (BA and 3-BBA systems), additional FTIR features consistent with borate-ester network formation were observed (Fig. 2b). Specifically, new peaks at 1429 and 1331 $cm^{-1}$ are attributed to the tetrahedral borate ester (B—O—C) environment, while changes in the —OH region (broadening and intensity reduction) indicate the partial consumption of hydroxyl groups due to crosslinking and stronger intermolecular interactions. The band near 842 $cm^{-1}$ is attributed to B—O stretching associated with residual borate species (*e.g.*, $B(OH)^{4-}$-type motifs), further supporting the successful incorporation of boron chemistry into the PVA network.[45] The FTIR results support a multicomponent network in which covalent/coordination-type borate linkages cooperate with extensive hydrogen bonding. Such a hybrid network is expected to increase the microenvironment rigidity and suppress the segmental motions of the polymer and guest, which are important structural prerequisites for stabilizing triplet excitons and enabling efficient RTP in organic matrices.

Optical transparency measurements further reflected how guest loading and network construction modified the film microstructure (Fig. 2c). Neat PVA showed a moderate transmittance of 55% in the visible region (400–700 nm), consistent with its homogeneous amorphous morphology. Incorporation of the coumarin derivative reduced transmittance (PVA-A: about 12%, PVA-B: about 16%, and PVA-C: about 30%), which can be attributed to two combined effects: intrinsic absorption from the aromatic coumarin chromophore (particularly toward the near-UV/blue edge) and increased light scattering caused by local heterogeneity introduced by the additive. The PVA-A-BA film shows a higher transmittance (32%) than PVA-A, while it remains less transparent than pure PVA, consistent with the idea that borate crosslinking reorganizes the microstructure and alters optical scattering. This transparency rebound after crosslinking is consistent with a more uniformly connected network that better disperses the guest and limits phase inhomogeneities, which is favorable for optical applications such as anti-counterfeiting labels, where legibility and appearance matter.

Mechanical robustness is essential for anti-counterfeiting labels and flexible encryption films because materials must withstand handling, bending, and long-term service without mechanical failure. To evaluate the influence of PVA molecular parameters on film mechanics, two commercial PVAs with identical alcoholysis degrees (99%) but different polymerization degrees were employed: 1799PVA (polymerization degree is about 1700) and 2499PVA (polymerization degree is about 2400). The numerical designations "1799" and "2499" therefore originate from the intrinsic polymer chain length, rather than differences in chemical composition. As shown in the stress-strain curves in Fig. 2(d), both 1799PVA- and 2499PVA-based PVA-G films exhibited good mechanical integrity after incorporation of the coumarin guest, indicating that coumarin doping does not intrinsically compromise the PVA matrix. However, clear differences arose from the degree of polymerization. Owing to its longer molecular chains and higher entanglement density, 2499PVA-A exhibits a higher breaking tensile strength (32.70 MPa), toughness of 63.82 $MJ/m^3$ and Young's modulus of 245.60 MPa, providing a mechanically robust baseline for further network regulation. In contrast, 1799PVA-based films, while slightly lower in ultimate strength, display a more balanced combination of strength and deformability, which is advantageous for flexible film processing and subsequent structural modification. Importantly, the shorter chain length of 1799PVA facilitated a more uniform dispersion of functional additives and more controllable crosslinking or coordination interactions. Based on the balance between mechanical robustness, flexibility, and processing stability, 1799PVA was selected as the primary polymer matrix for subsequent film construction and functional regulation. Upon further introduction of crosslinking agents or metal ions, the rigidity-toughness balance of the films can be predictably tuned by increasing the network density and restricting polymer chain mobility. Compared to PVA-A, crosslinked or ion-coordinated films exhibit increased stiffness but reduced plastic deformation. For example, PVA-A-TA and PVA-A-$CaCl_2$ show breaking tensile strengths of 26.09 MPa (Fig. 2e) and 40.85 MPa (Fig. 2f), respectively. Their corresponding toughness values decrease to 0.76 and 59.79 $MJ/m^3$ (Fig. 2h), whereas the Young's modulus increases to 1479.55 and 504.71 MPa (Fig. 2g), reflecting enhanced stiffness at the expense of extensibility. This trade-off is not detrimental but instead highlights the mechanical tunability of the PVA-based film system. By selecting appropriate PVA grades and third-component regulators, films with tailored mechanical profiles can be fabricated, ranging from tougher, highly deformable films suitable for repeated bending, to stiffer, abrasion-resistant films designed for high-durability anti-counterfeiting applications.

Thermal analysis (TGA/DTG) of PVA-A-BA demonstrated that the hybrid network retained good thermal integrity and that different components contributed to the staged weight loss events (Fig. 2i). The mass-loss feature near 120 °C is consistent with the removal of absorbed/bound water, typical of hydroxyl-rich polymers, potentially accompanied by a minor loss of small volatile boron-containing species. Subsequent decomposition of the coumarin component occurred at a higher temperature (about 300 °C), indicating that coumarin was immobilized in the cross-linked network. The main polymer decomposition occurred at a higher temperature (about 430 °C), indicating that the composite film maintained good overall thermal integrity. This staged decomposition behavior supports the suitability of processing and service conditions relevant to flexible labels and security films.

## Optical Properties of the PVA Composites

Afterglow photographs provide the most direct visual evidence of RTP performance and are therefore used to compare how guest structure and network design control the phosphorescence intensity and persistence. As shown in Fig. 3(a), all doped films display similar blue fluorescence under 365 nm irradiation, indicating that prompt emission is dominated by coumarin-

based excited singlet states. However, once the UV lamp was switched off, their afterglow behaviors diverged markedly: the G-B-doped film showed negligible phosphorescence, whereas the G-A- and G-C-doped films retained observable RTP (Video S1 in the electronic supplementary information, ESI), indicating a strong dependence of phosphorescence behavior on the molecular structure. The absence of phosphorescence in the G-B-doped films can be attributed to its 6,7-dihydroxy structure,

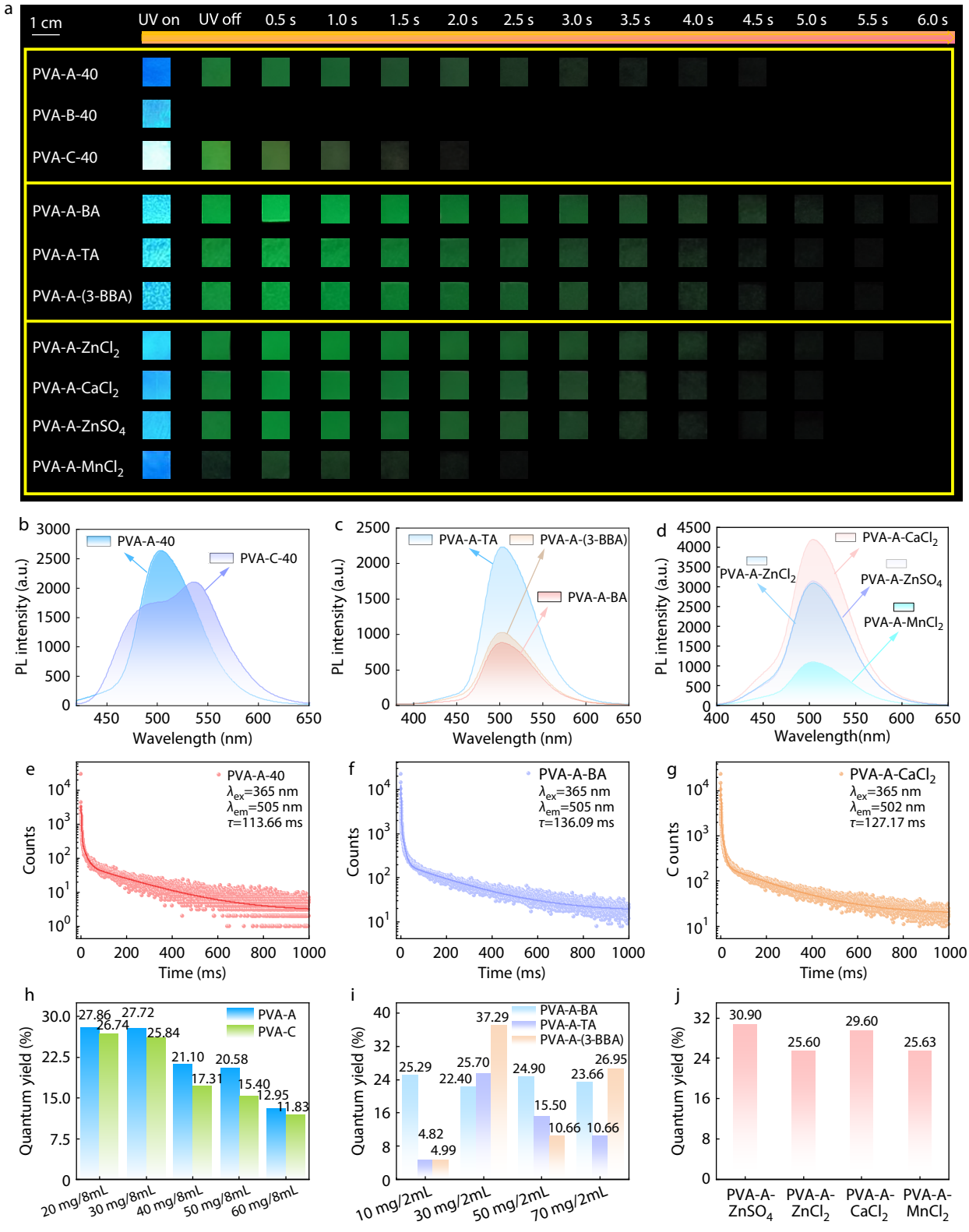


https://doi.org/10.1007/s10118-026-3717-3

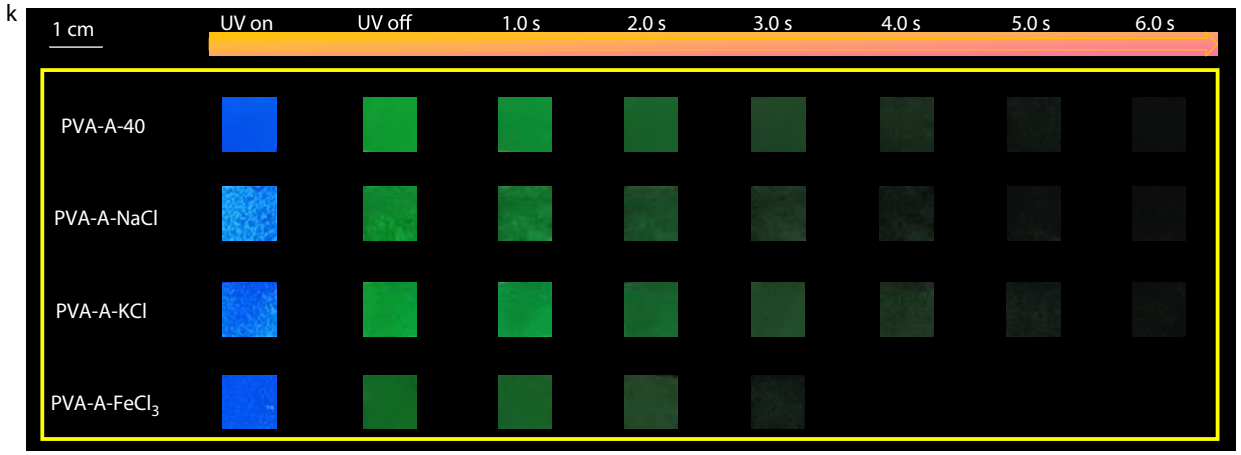


**Fig. 3** Multicolor optical response characteristics and phosphorescence performance of PVA composite films. (a) Photographs showing emission under 365 nm UV irradiation (prompt blue fluorescence) and after UV removal (green RTP afterglow) for PVA-G films, PVA-A-crosslinker films, and PVA-A-$M^{2+}$ films. Phosphorescence spectra of representative (b) binary PVA-A and PVA-C films, (c) PVA-A-crosslinker films, and (d) PVA-A-$M^{2+}$ films. The quantum yield of PVA-A film (40 mg/8mL ethanol solution), PVA-C film (40 mg/8mL ethanol solution), PVA-A-crosslinking agent film (mass ratio of 30:1:0.75), PVA-A-$M^{2+}$ film (mass ratio of 30:1.25:0.5). Phosphorescence attenuation curve of (e) PVA-A, (f) PVA-A-BA, and (g) PVA-A-$CaCl_2$ films. Photoluminescence quantum yields (PLQY) of (h) selected PVA-G, (i) PVA-A-crosslinker, and (j) PVA-A-$M^{2+}$ films. (k) Comparison of phosphorescence behavior of PVA-A films coordinated with metal ions of different valences ($Na^+$, $K^+$, $Fe^{3+}$) under UV irradiation and afterglow

which enables strong intramolecular hydrogen bonding and facilitates excited-state intramolecular proton transfer (ESIPT), introducing an efficient non-radiative decay pathway that suppresses intersystem crossing. In contrast, G-A and G-C lack ESIPT and instead favor a triplet-state population and stabilization through weaker hydrogen bonding or enhanced matrix interactions, thereby enabling observable RTP.[46,47] The G-A system exhibits a longer-lived afterglow than the G-C system, so optical evaluation of PVA-A was selected as the representative formulation for subsequent crosslinking and metal ion coordination. Because restricting molecular motion and strengthening intermolecular interactions are well known to suppress non-radiative decay, crosslinking was examined to evaluate whether network rigidification further enhances RTP. As shown in Fig. 3(a), the crosslinked PVA-A films show improved phosphorescence persistence to varying degrees, consistent with increased microenvironment rigidity and reduced triplet quenching. In particular, PVA-A-BA displays the most persistent afterglow, suggesting that the BA-derived network provides particularly effective confinement and stabilization of the triplet excitons in the PVA matrix (Video S1 in ESI). Quantitatively, the BA-crosslinked system (PVA-A-BA) exhibits a longer phosphorescence lifetime (127.17 ms versus 59.86 ms) and a lower non-radiative decay rate ($k_{nr}$ = 6.10×$10^{-3}$ $ms^{-1}$ versus 1.04×$10^{-2}$ $ms^{-1}$) than the TA system (Table S1 and Fig. S1 in ESI), corresponding to a about 1.7-fold reduction in $k_{nr}$ and a about 2.1-fold increase in lifetime, directly confirming the superior effectiveness of the BA-derived network in suppressing non-radiative decay.

Metal ion coordination was then explored as a second strategy to tune the triplet-state dynamics, since coordination can both rigidify the matrix and alter spin–orbit coupling and excited-state deactivation pathways. Most metal-ion-coordinated films exhibit enhanced phosphorescence relative to the uncoordinated PVA-A film, indicating that coordination generally benefits RTP in this system. An exception is $MnCl_2$, which weakens phosphorescence (Video S1 in ESI). This behavior is attributed to the specific electronic configuration of $Mn^{2+}$ ($3d^5$, half-filled shell), which can promote strong coupling with the coumarin triplet manifold through ligand-mediated interactions, opening a fast non-radiative relaxation channel and rapidly draining the triplet excitons back to the ground state.[48–51] Although quantitative ISC rate constants and phosphorescence lifetimes derived from transient spectroscopy are not available in this study, the observed trends are consistent with literature-reported structure–property relationships.

Steady-state emission spectra were used to quantify the wavelength and intensity differences and to clarify how the coumarin structure modulates the emissive triplet states. As shown in Fig. 3(b), PVA-A-40 exhibits a dominant emission peak at 505 nm, whereas PVA-C-40 shows two features at approximately 480 and 536 nm, indicating a different emissive-state distribution and microenvironment in the G-C system. However, the phosphorescence intensity of PVA-A was much stronger than that of PVA-C under comparable conditions, reinforcing the selection of G-A as the optimal guest for further network engineering. To isolate the effect of boron chemistry, the spectra of PVA-A films crosslinked with different boron-containing agents were compared to determine whether crosslinker identity primarily changes the emission color or emission efficiency. As shown in Fig. 3(c), the emission maxima remained broadly similar across the borate-crosslinked samples, implying that the emissive triplet state was essentially the same, while the phosphorescence intensities differed significantly. This indicates that crosslinker identity mainly regulates the efficiency of RTP (*e.g.*, by changing rigidity, hydrogen-bonding strength, or oxygen shielding) rather than fundamentally altering the emitting species; in this series, PVA-A-TA gives the strongest phosphorescence intensity. The spectra of metal-ion coordinated films were compared to establish how different cations influence the emission intensity while maintaining a similar emissive wavelength, consis-

tent with a shared coumarin-centered triplet origin. As shown in Fig. 3(d), all PVA-A-$M^{2+}$ films emit near 502 nm, suggesting that the emitting triplet state remains coumarin-based across the coordination series. However, the intensity varied strongly; PVA-A-$CaCl_2$ showed the highest phosphorescence intensity, whereas PVA-A-$MnCl_2$ was the weakest, consistent with coordination-enhanced rigidification for most ions and $Mn^{2+}$-induced triplet quenching through a fast non-radiative pathway. This quenching behavior is further supported by phosphorescence decay analysis, where $Mn^{2+}$-doped samples exhibit a drastic reduction in lifetime and a pronounced increase in the non-radiative decay rate ($k_{nr}$ = 16.97 $ms^{-1}$) compared to that of the undoped system ($k_{nr}$ = 6.94×$10^{-3}$ $ms^{-1}$) (Table S1 and Fig. S2 in ESI), confirming the formation of highly efficient non-radiative deactivation pathways in the presence of $Mn^{2+}$.

The phosphorescence decay curve is the core basis for characterizing the luminescence properties of phosphorescent materials. As shown in Fig. 3(e), the PVA-A film exhibits a long phosphorescence lifetime ($\tau$ = 113.66 ms), indicating efficient intersystem crossing enabled by the $\pi$-conjugated structure of coumarin incorporated into the PVA matrix. In addition, the crosslinked rigid environment effectively suppressed molecular motion, thereby inhibiting non-radiative decay and aggregation-induced quenching. Upon the introduction of the crosslinking agent BA (Fig. 3f), the phosphorescence lifetime was further prolonged to $\tau$ = 136.09 ms. This enhancement demonstrates that BA forms a dense and stable hydrogen bond network with the PVA molecular chain, which significantly limits the free movement of the PVA chain segment as well as molecular vibration and rotation, thereby effectively suppressing the non-radiative decay of the triplet excited state and reducing the energy loss of the excited state. Similarly, the PVA-A-$CaCl_2$ film (Fig. 3g) showed a markedly extended phosphorescence lifetime ($\tau$ = 127.17 ms) compared to PVA-A. This improvement indicates that $Ca^{2+}$ ions coordinate with PVA molecular chains, constraining chain flexibility and decreasing vibrational relaxation rates, which effectively blocks non-radiative decay pathways and stabilizes the triplet excited state. Although lifetime measurements were primarily performed on representative compositions, the influence of concentration on excited-state dynamics can be inferred from the general photophysical principles. Increasing the guest concentration enhances intermolecular interactions, which facilitate non-radiative energy transfer and concentration quenching, and is therefore expected to shorten both fluorescence and phosphorescence lifetimes. In contrast, the introduction of crosslinking or metal-ion coordination effectively rigidifies the microenvironment and suppresses non-radiative decay, leading to prolonged phosphorescence lifetimes.

Photoluminescence quantum yield (PLQY) measurements were performed to quantitatively compare the emission efficiency and verify whether guest selection, crosslinking, and metal-ion coordination suppress non-radiative decay in the RTP films. As shown in Fig. 3(h), the PVA-A films exhibited higher PLQYs, confirming that the coumarin structure and its microenvironment in PVA strongly controlled the overall emissive efficiency. Fig. 3(i) further shows that introducing different crosslinkers markedly alters PLQY, indicating that network construction actively tunes the rigidity organization and oxygen accessibility around the chromophore, thereby modulating radiative–non-radiative competition. Similarly, Fig. 3(j) demonstrates that metal-ion coordination generally increases the PLQY by strengthening confinement and intermolecular interactions, whereas $Mn^{2+}$ gives the lowest PLQY due to efficient excited-state quenching, consistent with rapid non-radiative deactivation enabled by its high-spin $d^5$ electronic configuration. To further investigate the effect of metal ion valence on the RTP performance, monovalent ($Na^+$, $K^+$) and trivalent ($Fe^{3+}$) ions were introduced for comparison (Fig. 3k). All the samples exhibited observable phosphorescence, indicating that the RTP behavior was preserved across different valence states. However, $Na^+$ and $K^+$ showed negligible enhancement, suggesting weak coordination interactions, whereas $Fe^{3+}$ led to a slight decrease in the emission intensity, likely due to enhanced non-radiative decay. These results highlight that divalent ions provide a more favorable balance between coordination-induced rigidification and the suppression of quenching pathways.

## Environmental Responsiveness, Stability, and Repeatability of the PVA Composites

To evaluate the environmental responsiveness and stability of the films, their swelling behavior and photostability were systematically investigated. As shown in Fig. 4(a), the PVA-A-$CaCl_2$ film exhibits a rapid increase in the swelling ratio, reaching 36.19% within 4 s of water exposure, reflecting the hydrophilic nature of the PVA matrix. Correspondingly, the emission behavior evolved significantly during the swelling process (Fig. 4b). Given the strong water sensitivity observed in the swelling experiments, we further evaluated humidity-dependent photophysical behavior. The RTP properties of the PVA-A-$CaCl_2$ films were examined under 30% and 50% relative humidity (RH) conditions. Both humidity levels led to reduced phosphorescence intensity and shortened lifetime, while the PLQY showed a slight increase (Figs. S3–S5 in ESI). The observed decrease in lifetime indicates an overall increase in the total decay rate ($k_r$ + $k_{nr}$), whereas the change in PLQY reflects a redistribution between the radiative and non-radiative channels. This behavior is attributed to the water-induced modulation of hydrogen-bonding interactions within the polymer network, which alters the excited-state relaxation dynamics and changes the balance between the radiative and non-radiative decay pathways. The emission properties were largely restored after drying (Fig. S6 in ESI), confirming the reversible nature of the moisture-induced effects and the good humidity tolerance of the films.

With increasing immersion time, the phosphorescence intensity gradually decreases and becomes nearly undetectable at higher swelling levels. This attenuation is attributed to the water-induced disruption of hydrogen-bonding interactions and increased molecular mobility, which enhance non-radiative decay and quench triplet excitons. Notably, after drying, the phosphorescence fully recovered to its original intensity, indicating that the luminescence performance was reversible and no permanent structural degradation occurred. In addition, the photostability of the films was evaluated under continuous UV irradiation (365 nm) (Fig. 4c). No

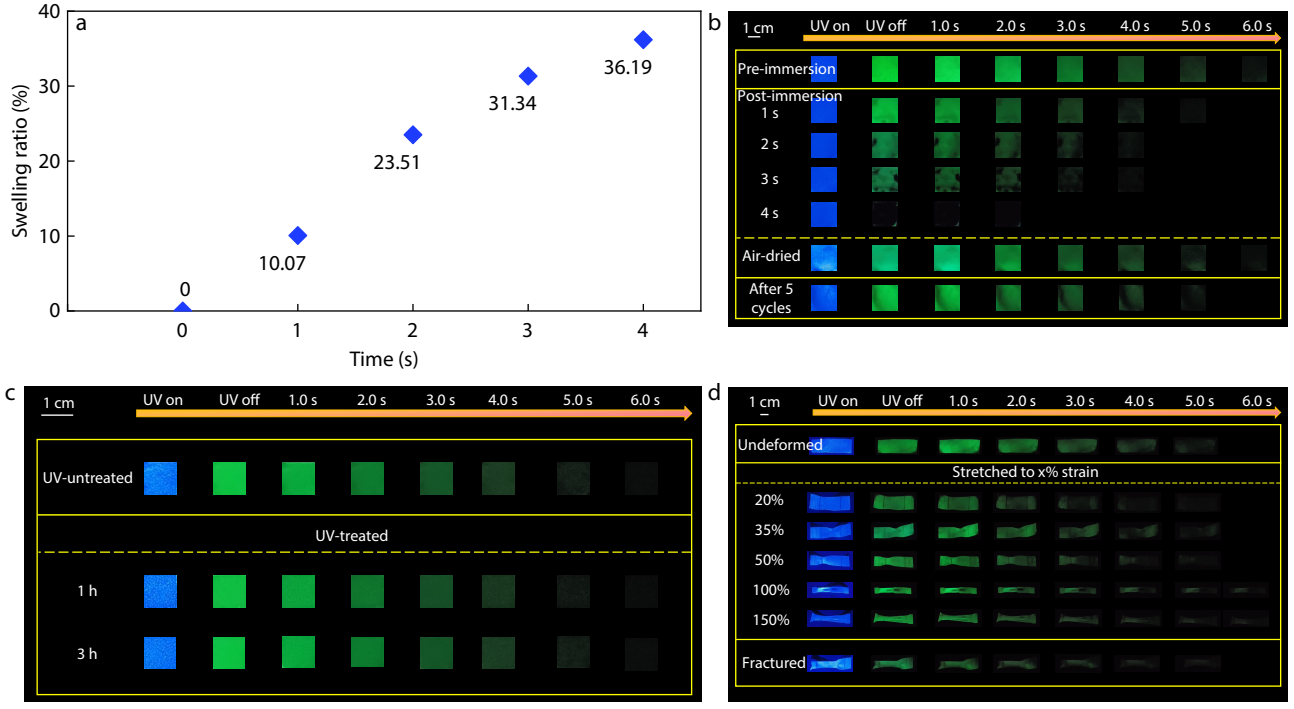


**Fig. 4** Environmental stability and swelling-responsive phosphorescence behavior of PVA-A-$CaCl_2$ films. (a) Swelling ratio of PVA-A-$CaCl_2$ films as a function of immersion time; (b) Evolution of emission under 365 nm UV and afterglow during immersion-drying cycles, demonstrating reversible phosphorescence recovery; (c) UV photostability of PVA-A-$CaCl_2$ films before and after 1 h and 3 h irradiation, showing negligible degradation; (d) Evolution of emission under different tensile strains (20%–150%).

significant change in the emission intensity or afterglow behavior was observed after prolonged irradiation (1–3 h), demonstrating good resistance to UV-induced degradation. The phosphorescence decay profile after prolonged UV exposure (3 h) further confirmed the stable emission kinetics, with a phosphorescence lifetime of 37.61 ms (Fig. S7 in ESI), indicating negligible photodegradation and excellent excitation cycle repeatability. Furthermore, the influence of mechanical deformation on the phosphorescence was investigated (Fig. 4d). With increasing tensile strain (20%–150%), the emission intensity gradually decreased because of the disruption of the rigid microenvironment and enhanced non-radiative decay. Nevertheless, the afterglow remained clearly observable even at high strain levels, and luminescent behavior was maintained prior to fracture, demonstrating good repeatability and mechanical tolerance. Quantitative analysis under different tensile states shows that the phosphorescence lifetime remains in the range of 36.49 ms (50% strain), 27.85 ms (100% strain), and 30.41 ms (fractured state), respectively (Figs. S8a–S8c in ESI), confirming that the emissive triplet state dynamics were largely preserved even under severe mechanical deformation. These results confirm that the PVA-based RTP system maintained stable excited-state relaxation dynamics under repeated photonic and mechanical perturbations.

To determine whether guest loading tunes emission color or primarily affects emission efficiency, we first compared the emission spectra of PVA-A films prepared with different G-A doping concentrations. As shown in Fig. 5(a), the peak position remains essentially unchanged, between 400–450 nm, across the concentration gradient, indicating that the emissive state is the same, while the intensity varies significantly, reflecting concentration-dependent changes in radiative output. To evaluate whether the network construction alters the intrinsic emissive state, PVA-A films crosslinked with different agents were examined. In Fig. 5(b), crosslinking produces minimal changes in the emission wavelength (450–500 nm) with no pronounced red shift, indicating that crosslinking mainly regulates the microenvironment rigidity pathways rather than creating a new emitting species; the primary effect is reflected in changes in emission intensity among different crosslinkers, with the PVA-A-TA film exhibiting the strongest fluorescence emission intensity. To verify that the concentration-intensity relationship is not specific to a single coumarin guest, we performed the same analysis on the G-C-doped PVA films. As presented in Fig. 5(c), the emission maxima are broadly consistent across concentrations, but the intensity depends strongly on loading; the film prepared at 40 mg/8 mL ethanol solution exhibits the strongest emission, suggesting an optimal guest concentration that maximizes emission before concentration quenching becomes significant. The different trends in emission intensity and PLQY arise from their distinct physical meanings. The emission intensity reflects the total radiative output, which is determined by both the number of emissive centers and their efficiency, whereas PLQY represents the intrinsic emission efficiency. At low concentrations, increasing the guest loading increases the number of emissive centers, leading to a higher intensity with minimal change in efficiency. With a further increase in concentration, enhanced intermolecular interactions introduce non-radiative pathways, causing a monotonic decrease in the PLQY. Nevertheless, in the intermediate range, the increase in the emissive centers outweighs the efficiency loss,

https://doi.org/10.1007/s10118-026-3717-3

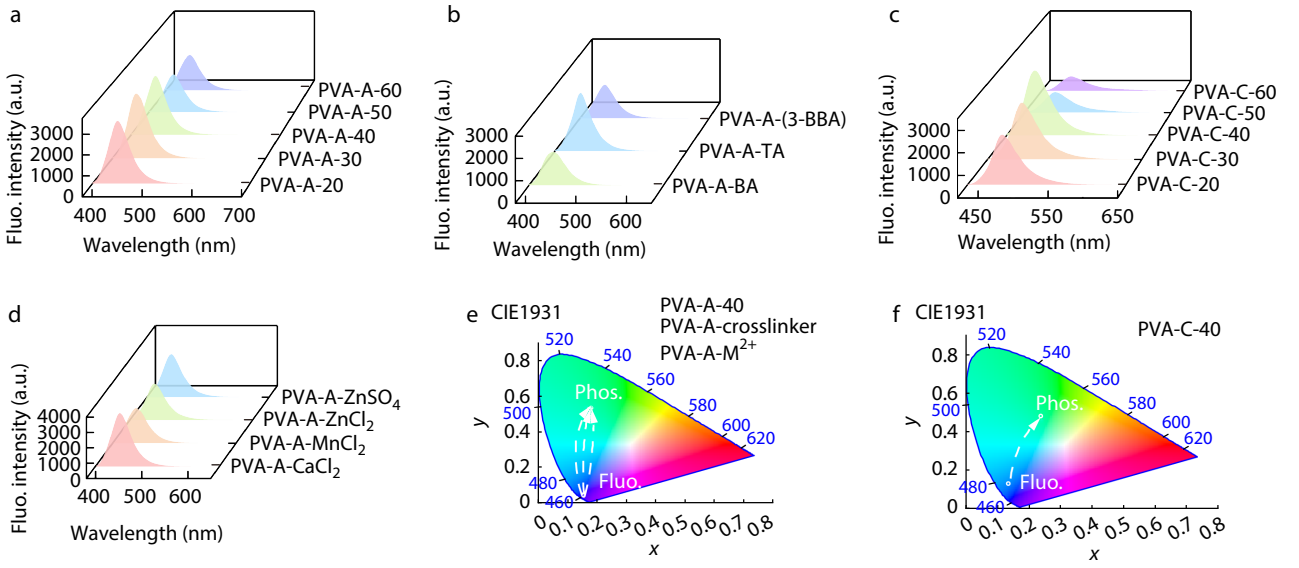


**Fig. 5** Emission spectra and color coordinates of RTP composite films. Emission spectra of (a) PVA-A films prepared with different G-A concentration gradients (G-A doping concentration gradient: 20 mg/8mL ethanol solution, 30 mg/8mL ethanol solution, 40 mg/8mL ethanol solution, 50 mg/8mL ethanol solution, 60 mg/8mL ethanol solution), (b) PVA-A-crosslinker films (mass ratio: 30:1:0.75), (c) PVA-C films with different G-C concentration gradients in 8 mL ethanol solution, and (d) PVA-A-$M^{2+}$ films (mass ratio: 30: 1.25: 0.5). CIE 1931 chromaticity diagrams of (e) PVA-A (40 mg/8mL ethanol solution), PVA-A-crosslinker (mass ratio of 30:1:0.75), PVA-A-$M^{2+}$ (mass ratio of 30:1.25:0.5) and (f) PVA-C film.

resulting in continued intensity growth. At higher concentrations, non-radiative decay and self-absorption dominate, leading to a decrease in the emission intensity.[52–54]

To probe the role of metal-ion coordination in modulating the emission, we compared the spectra of the PVA-A-$M^{2+}$ films. Fig. 5(d) shows that coordination does not cause an obvious shift in the emission wavelength, but strongly affects the intensity. Among the tested ions, $CaCl_2$ coordination provided a particularly pronounced enhancement, consistent with improved confinement and reduced non-radiative decay in the matrix. The CIE chromaticity analysis provides an intuitive, device-relevant description of the color evolution between prompt and delayed phosphorescence. As shown in Figs. 5(e) and 5(f), the emission coordinates indicate a clear conversion from blue-purple fluorescence to green phosphorescence across the representative films, demonstrating that the afterglow color is largely preserved, while intensity is the main tunable parameter through concentration, crosslinking, and coordination.

## Processability and Time-dependent Multi-level Information Encryption

PVA-based RTP films exhibited excellent processability and patternability. As shown in Fig. S9(a) (in ESI), the films can be readily fabricated into diverse two-dimensional patterns (*e.g.*, star, heart, clover, snowflake, and flower shapes) and three-dimensional structures (*e.g.*, molded cups). These structures maintained uniform morphology and integrity, demonstrating good mechanical flexibility and moldability. In addition, the material supports fine-pattern construction with distinguishable luminescence signals under UV irradiation (Fig. S9b) (in ESI), indicating their potential for use in high-resolution optical information displays.

Building on this processability, the practical potential of these RTP composites for multi-level encryption was further demonstrated with digit- and matrix-based patterns that reveal different information at different illumination and delay conditions. As shown in Fig. 6(a), the PVA composite films were cut and assembled into a four-digit display. Under daylight, all segments appear nearly identical (transparent); therefore, no information can be read. Upon 365 nm UV irradiation, some segments show bright blue fluorescence, and the display presents an intentionally misleading code ("8086"). When the UV lamp is switched off, the fluorescence disappears immediately while the RTP segments continue to emit green afterglow, enabling time-gated decoding: after a short delay ($t \approx 1$ s) the displayed number changes to "2026," and after a longer delay ($t \approx 3$ s) it evolves further to "2025" (Video S2 in ESI). This proof-of-concept confirms that the same physical label can output multiple layers of information, depending on the observation time window. However, a simply patterned afterglow can still be vulnerable if an attacker can repeatedly observe the label under controlled timing. Therefore, to increase security, we designed a higher-level encryption system that combines time resolution with binary coding.

To achieve multi-level, time-programmed encryption, we leveraged the distinct time-dependent emission behaviors of fluorescent-only and RTP-active components (PVA-C and PVA-A-BA) and implemented an 8-bit ASCII binary coding scheme in an 8 × 4 encryption matrix (Fig. 6b). In daylight, the information remains hidden because the films are transparent and the pixel array provides no readable contrast. Under UV light, a part of the matrix emits blue fluorescence, assigning the luminescent point a value of 1 and the non-luminescent point a value of 0. This response yields a binary output that decodes to a decoy string ("OWOO") under ASCII rules. After removing the UV source, only the RTP pixels continued to glow (green), producing a different intermediate output

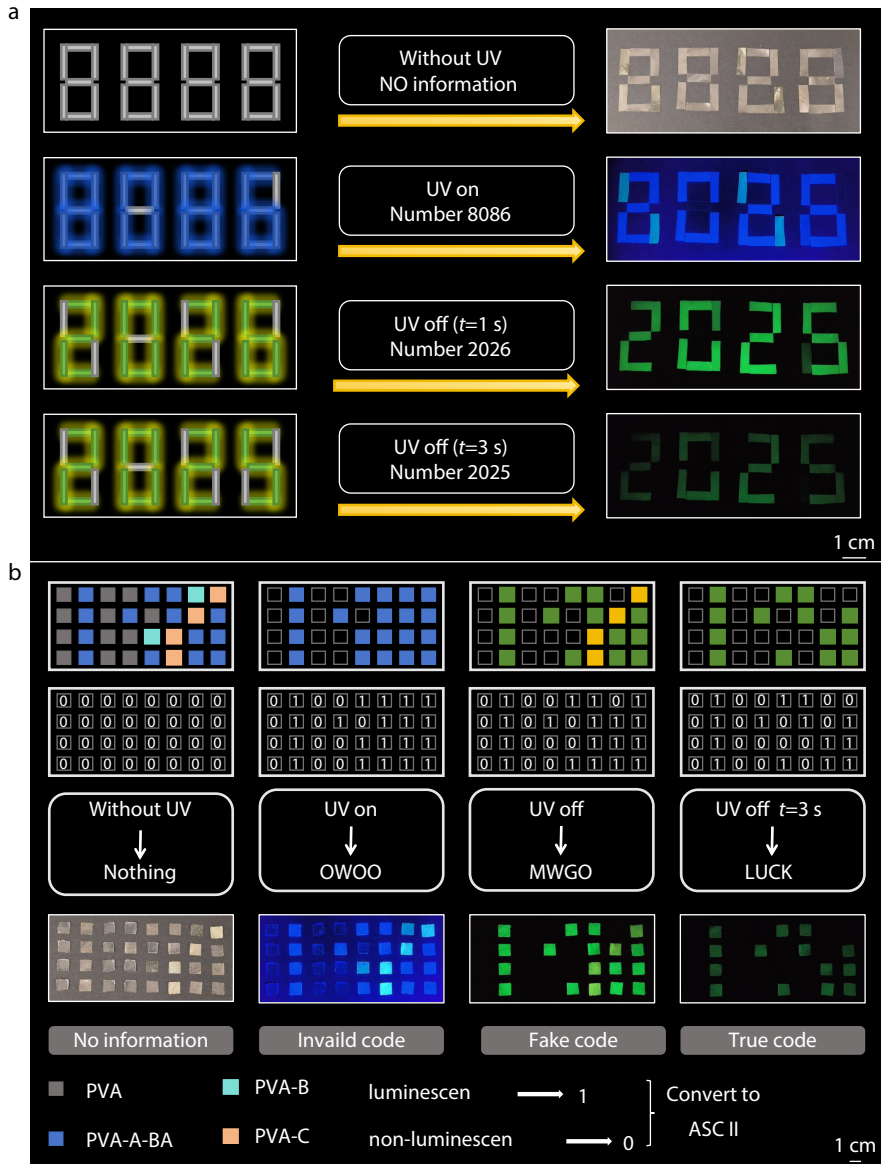


**Fig. 6** Two-dimensional, time-gated information encryption enabled by multicomponent PVA-G RTP films. (a) Time-dependent digit display assembled from PVA-A (40 mg/8mL ethanol solution), PVA-B (40 mg/8mL ethanol solution), PVA-A-BA (mass ratio of 30:1:0.75), and PVA-A-$CaCl_2$ (mass ratio of 30:1.25:0.5), demonstrating sequential message readout governed by differences in phosphorescence lifetime. (b) Time-resolved multi-level encryption matrix constructed from PVA (50 mg/mL), PVA-B (40 mg/8mL ethanol solution), PVA-C (40 mg/8mL ethanol solution), and PVA-A-BA (mass ratio of 30:1:0.75), enabling decoy and true information outputs through UV excitation and delayed afterglow decoding.

("MWGO") that still did not reveal the true message. When the system is read using the correct time-gated protocol (UV excitation followed by a defined delay for about 3 s), the persistent pixels form the correct 8-bit codes: 01001100, 01010101, 01000011, and 01001011, which decode to the true information "LUCK" (Video S2 in ESI). This strategy requires both knowledge of the coding standard and the correct time-resolved readout procedure while also providing multiple plausible decoy outputs. The combination of concealment under daylight, fluorescence-based misdirection under UV, and time-gated RTP decoding substantially increases the difficulty of unauthorized decryption, rendering the proposed multi-level encryption lattice a high-security platform for information storage and anti-counterfeiting.

## CONCLUSIONS

This work demonstrates a simple and effective ternary strategy for flexible RTP films: PVA as the host matrix, coumarin derivatives as the emissive guests, and a third component (boric acid, tannic acid, or metal ions) as a microenvironment regulator. Spectroscopic and property characterizations confirmed that coumarin incorporation was retained within the PVA framework and that introducing the third component markedly strengthened phosphorescence by simultaneously increasing matrix rigidity and reducing non-radiative decay, while maintaining the integrity of the PVA framework. The three modulation strategies exhibit distinct structure–property relationships. Covalent crosslinking with boric acids (BA and 3-BBA) forms

dense borate/borate-ester crosslinked networks that restrict guest motion and improve the resistance to oxygen quenching, resulting in enhanced phosphorescence intensity and lifetime. Hydrogen-bonding networks induced by tannic acid (TA) provide a moderately rigid microenvironment that suppresses vibrational/rotational dissipation and mitigates quencher interference, leading to improved RTP efficiency. Metal-ion coordination ($Ca^{2+}$ and $Zn^{2+}$ salts) offers an additional route to network reinforcement through coordination/hydrogen-bond-assisted crosslinking and modulation of the guest electronic environment, which can facilitate triplet formation and stabilize emissive triplet states. In contrast, $Mn^{2+}$ introduces efficient non-radiative deactivation and weakens RTP, highlighting the importance of ion selection. The tunable lifetime and color evolution enable practical, time-gated, and multi-level information encryption, including dynamic digit displays and ASCII-based matrix encryption with decoy outputs and a delayed true code readout. More broadly, this ternary strategy establishes a general design principle for RTP materials in which localized rigidification of emissive centers is achieved without compromising the global flexibility and processability of the polymer matrix. By decoupling microscopic photophysical regulation from macroscopic mechanical properties, this approach effectively resolves the long-standing trade-off between strong phosphorescence and desirable mechanical characteristics. This modular host-guest-regulator design offers a versatile platform for engineering processable RTP composites with programmable optical outputs, providing a promising material basis for advanced anti-counterfeiting and high-security information storage.

## Conflict of Interests

The authors declare no interest conflict.

## Electronic Supplementary Information

Electronic supplementary information (ESI) is available free of charge in the online version of this article at http://doi.org/10.1007/s10118-026-3717-3.

## Data Availability Statement

Data supporting the findings of this study are available from the corresponding author upon reasonable request. Contact information for the authors: zhangjianfu@cust.edu.cn.

## ACKNOWLEDGMENTS

This study was financially supported by the National Natural Science Foundation of China (No. 22275023). J.L. is grateful for the support of the Jilin Science and Technology Association (No. BST202511). J.Z. and X.L. also acknowledge the National Undergraduate Innovation and Entrepreneurship (No. 202510186037).

## REFERENCES

1 Shi, L.; Ding, L.; Zhang, Y.; Lu, S. Application of room-temperature phosphorescent carbon dots in information encryption and anti-counterfeiting. *Nano Today* **2024**, *55*, 102200.
2 Chen, X.; Han, G.; Ren, P.; Lyu, Q.; Li, M.; Zhang, L.; Zhu, J. Shape memory photonic gels enable reversible regulation of photoluminescence: towards multiple anti-counterfeiting. *Chem. Eng. J.* **2022**, *446*, 136879.
3 Xu, L. R.; Wang, J. Y.; Huang, J. T.; He, Q. Y.; Lu, S. L.; Feng, D. C.; Ma, Z. T.; Yuan, Z. K.; Yang, Y. Z.; Chen, X. D. Multi-mode polarized luminescent au-nanorod polymer composites for advanced optical anti-counterfeiting. *Chinese J. Polym. Sci.* **2025**, *43*, 2118–2127.
4 Zhang, X.; Cheng, Y.; You, J.; Zhang, J.; Wang, Y.; Zhang, J. Irreversible humidity-responsive phosphorescence materials from cellulose for advanced anti-counterfeiting and environmental monitoring. *ACS Appl. Mater. Interfaces* **2022**, *14*, 16582–16591.
5 Zhao, W.; He, Z.; Tang, B. Z. Room-temperature phosphorescence from organic aggregates. *Nat. Rev. Mater.* **2020**, *5*, 869–885.
6 Wang, Q.; Xu, H.; Li, X.; Qu, D. H. Temporal dynamic room-temperature phosphorescent materials with multicolor tunability for time-dependent information encryption. *CCS Chem.* **2026**, *8*, 2513–2522.
7 Yang, L.; Zhang, Q.; Ma, Y.; Li, H.; Sun, S.; Xu, Y. Stimulus-responsive room-temperature phosphorescence with tunable color for time-resolved advanced dynamic anti-counterfeiting. *Chem. Eng. J.* **2024**, *490*, 151679.
8 Shi, M.; Gao, Q.; Chen, M.; Lv, Z.; Rao, J.; Chen, G.; Lü, B.; Qi, W.; Ren, J.; Peng, F. Hierarchical luminescence center coupling enables time-dependent phosphorescence color from self-protective carbonized polymer dots. *Nat. Commun.* **2025**, *16*, 7473.
9 Wu, Y.; Zhou, W.; Qiu, Y.; Wang, S.; Liu, J.; Chen, Y.; Xu, X.; Liu, Y. 4D assembly of time-dependent lanthanide supramolecular multicolor phosphorescence for encryption and visual sensing. *Adv. Sci.* **2025**, *12*, 2415418.
10 Zhu, X.; Huang, J.; Lin, Y.; Wang, B.; Lu, S.; Chen, S.; Lan, Z.; Feng, D.; Gu, X.; Ma, Z.; Yuan, Z.; Yang, Y.; Chen, X. Laser-engraved multilevel encryption enabled by FRET-based tunable multicolor polymeric afterglow materials. *Sci. China Mater.* **2025**, *68*, 4430–4439.
11 Cai, S.; Yao, X.; Ma, H.; Shi, H.; An, Z. Manipulating intermolecular interactions for ultralong organic phosphorescence. *Aggregate* **2023**, *4*, e320.
12 Guan, Z.; Tang, Z.; Deng, J.; Zheng, Y.; Li, H.; Liu, X. Multi-color pure organic room temperature phosphorescent materials with long lifetime and high efficiency. *Adv. Funct. Mater.* **2024**, *34*, 2310198.
13 Li, Q.; Zhou, M.; Yang, M.; Yang, Q.; Zhang, Z.; Shi, J. Induction of long-lived room temperature phosphorescence of carbon dots by water in hydrogen-bonded matrices. *Nat. Commun.* **2018**, *9*, 734.
14 Zhou, Y.; Qu, L.; Yi, S.; Wang, C.; Chen, X.; Tang, S.; Tang, H.; Li, Y.; Wang, K.; Zhao, Y.; Yang, C. Dual promotion of phosphorus groups for ultralong room temperature phosphorescence with high efficiency. *Adv. Opt. Mater.* **2023**, *11*, 2201904.
15 Wang, K.; Qu, L.; Yang, C. Long-lived dynamic room temperature phosphorescence from carbon dots based materials. *Small* **2023**, *19*, 2206429.
16 Shu, H.; Liu, Y.; Chen, L.; Cheng, Z.; Wang, X.; Wu, X.; Tong, H.; Wang, L. Suppression of nonradiative transitions of triplet excitons *via* a fused/non-fused strategy for realizing efficient room-temperature phosphorescence. *J. Mater. Chem. C* **2023**, *11*, 10398–10403.
17 Ding, B.; Ma, X.; Tian, H. Recent advances of pure organic room temperature phosphorescence based on functional polymers. *Acc. Mater. Res.* **2023**, *4*, 827–838.

## Graphical Abstract

### Synergistically Enhanced Time-resolved Dual-mode Emission in Flexible Poly(vinyl alcohol) Films for Dynamic Information Encryption

Xiao-Ya Liu, Jin-Fang Liu, Ahmed Olalekan Omoniyi, and Jian-Fu Zhang

*Changchun University of Science and Technology; Zhongshan Institute of Changchun University of Science and Technology*

This study proposes a three-component strategy for fabricating flexible RTP thin films. The core innovation is to achieve time gating and multi-level information encryption through an adjustable lifetime and color evolution.

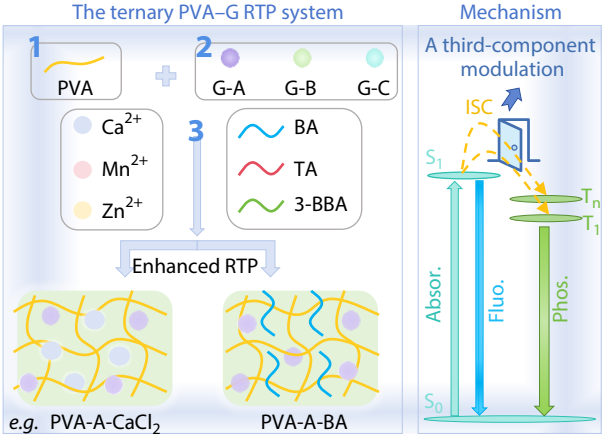


*Chinese J. Polym. Sci. 2026, 44, 3476–3489* *https://doi.org/10.1007/s10118-026-3717-3*

18 Gao, Q.; Shi, M.; Rao, J.; Su, Z.; Chen, G.; Lü, B.; Bian, J.; Peng, F. Fully exploiting clusterization-triggered room temperature phosphorescence of cellulose by stepwise rigidification for long-lived and excitation wavelength-dependent afterglows. *Adv. Funct. Mater.* **2024**, *34*, 2403977.
19 Yang, G.; Hao, S.; Deng, X.; Song, X.; Sun, B.; Hyun, W. J.; Li, M. D.; Dang, L. Efficient intersystem crossing and tunable ultralong organic room-temperature phosphorescence via doping polyvinylpyrrolidone with polyaromatic hydrocarbons. *Nat. Commun.* **2024**, *15*, 4674.
20 Liang, Z.; Wei, M.; Zhang, S.; Huang, W.; Shi, N.; Lv, A.; Ma, H.; He, Z. Activating molecular room-temperature phosphorescence by manipulating excited-state energy levels in poly(vinyl alcohol) matrix. *ACS Appl. Mater. Interfaces* **2023**, *15*, 35534–35542.
21 Zhang, S.; Yao, W.; Lv, A.; Liu, K.; Zhang, Y.; Zhou, C.; Ma, H.; Shi, H.; An, Z. Achieving highly efficient long-wavelength phosphorescence emission of large singlet-triplet energy gap materials by host-guest doping. *Sci. China Chem.* **2024**, *67*, 1922–1928.
22 Yang, G.; He, P.; Bai, J.; Qin, F.; Wang, X.; Yu, X.; Qian, S.; Yao, Y.; Ren, L. pH-driven chromophore amplification enables high-efficiency phosphorescent carbon dots. *Talanta* **2026**, *297*, 128544.
23 Xiao, Y.; Li, J.; Song, Z.; Liao, J.; Shen, M.; Yu, T.; Huang, W. 3D printable materials with visible light triggered photochromism and room temperature phosphorescence. *J. Am. Chem. Soc.* **2025**, *147*, 20372–20380.
24 Wang, C.; Ding, Y.; Wang, X.; Huang, W.; An, Z. Organic room temperature phosphorescence by confining isolated chromophores. *Acc. Mater. Res.* **2025**, *6*, 1383–1395.
25 Xia, S.; Lu, H.; He, J.; Lei, Y.; Dai, W.; Chai, Y.; Song, Y.; Huang, X.; Wu, H. Ester-induced energy-level modulation and host–guest synergy in visible-light-excited organic room-temperature phosphorescence. *Chem. Eng. J.* **2026**, *529*, 172711.
26 Zhang, H.; Wu, S.; Liang, Y.; Zhang, Z.; Wei, H.; Yang, Q.; Hu, P.; Liu, C.; Yang, Z.; Zheng, C.; Shi, G.; Chi, Z.; Xu, B. Enabling efficient and ultralong room-temperature phosphorescence from organic luminogens by locking the molecular conformation in polymer matrix. *Chem. Eng. J.* **2024**, *497*, 154949.
27 Wen Deng, W.; Ping Zhang, Z.; Zhi Rong, M.; Qiu Zhang, M. Versatile room temperature phosphorescence polymer with luminophore content as low as 0.05 wt%. *Chem. Eng. J.* **2024**, *495*, 153443.
28 Wu, B.; Guo, N.; Xu, X.; Xing, Y.; Shi, K.; Fang, W.; Wang, G. Ultralong and high-efficiency room temperature phosphorescence of organic-phosphors-doped polymer films enhanced by 3D network. *Adv. Opt. Mater.* **2020**, *8*, 2001192.
29 Chen, H.; Dong, M.; Wu, Y.; Shan, J.; Long, Z.; Gao, Y.; Gu, L. Chain-stiffening enhanced ultralong organic phosphorescence in high glass transition temperature polymers. *J. Mater. Chem. C* **2025**, *13*, 14458–14464.
30 Chen, H.; Qian, Z.; Qian, H. J.; Dong, M.; Zhang, Y.; Shan, J.; Huo, W.; Lv, A.; Guo, J.; Ma, H.; An, Z.; Huang, W.; Gu, L. Stretchable and flexible room-temperature phosphorescence copolymers based on microphase separation. *Chem. Mater.* **2024**, *36*, 5100–5109.
31 Wang, Y.; Ye, W.; Cao, T.; Wang, C.; Meng, H.; Gao, Z.; Wang, C. Metal-Free organic polymeric room temperature phosphorescence system with multi-colour and ultralong lifetime. *Chem. Eng. J.* **2024**, *481*, 148642.
32 Li, T.; Wang, Y.; Li, S.; Liu, X.; Sun, J. Mechanically robust, elastic, and healable ionogels for highly sensitive ultra-durable ionic skins. *Adv. Mater.* **2020**, *32*, 2002706.
33 Zou, R.; Yu, Y.; Pan, H.; Zhang, P.; Cheng, F.; Zhang, C.; Chen, S.; Chen, J.; Zeng, R. Cross-linking induced emission of polymer micelles for high-contrast visualization level 3 details of latent fingerprints. *ACS Appl. Mater. Interfaces* **2022**, *14*, 16746–16754.
34 Yao, W.; Huang, J.; Liu, W.; Ma, J.; Li, J.; Liu, D.; Yang, Y.; Liu, X.; Tian, Q.; Liu, W. Thermal/NIR activated self-healing polyurethane with shape memory toward multi-level encryption. *Chem. Eng. J.* **2025**, *522*, 167643.
35 Wei, X.; Gou, Z.; Ye, J.; Shi, L. H.; Zhao, J.; Yang, L.; Zhang, L.; Zhang, K.; Jia, R. Stretchable full-color phosphorescent PVA-

based ionogels for multimodal sensing-visual integration applications. *Adv. Sci.* **2025**, *12*, 2411229.
36 He, J.; He, Y.; Chen, Y.; Zhang, X.; Hu, C.; Zhuang, J.; Lei, B.; Liu, Y. Construction and multifunctional applications of carbon dots/PVA nanofibers with phosphorescence and thermally activated delayed fluorescence. *Chem. Eng. J.* **2018**, *347*, 505–513.
37 Li, D.; Yang, Y.; Yang, J.; Fang, M.; Tang, B. Z.; Li, Z. Completely aqueous processable stimulus responsive organic room temperature phosphorescence materials with tunable afterglow color. *Nat. Commun.* **2022**, *13*, 347.
38 Liu, M.; Mao, Z.; Wang, Y.; Kong, W.; Huang, J.; Li, W.; Yang, Z.; Huang, X.; Zou, W.; Yu, H. Activating ultralong room-temperature phosphorescence of mono-ring arylboronic acid by hydrogen bond for tunable afterglow color and stimulus response. *Small* **2025**, *21*, 2407079.
39 Li, M.; Ling, K.; Shi, H.; Gan, N.; Song, L.; Cai, S.; Cheng, Z.; Gu, L.; Wang, X.; Ma, C.; Gu, M.; Wu, Q.; Bian, L.; Liu, M.; An, Z.; Ma, H.; Huang, W. Prolonging ultralong organic phosphorescence lifetime to 2.5 s through confining rotation in molecular rotor. *Adv. Opt. Mater.* **2019**, *7*, 1800820.
40 Luo, W.; Zhou, J.; Nie, Y.; Li, F.; Cai, S.; Yin, G.; Chen, T.; Cai, Z. Hydrogen-bonded organic frameworks enabling highly robust aqueous phase ultralong room-temperature phosphorescence. *Adv. Funct. Mater.* **2024**, *34*, 2401728.
41 Chen, X.; Tian, X.; Chen, L.; Cui, M.; Zhang, Q.; Feng, Y.; Jia, C. Metal coordination-mediated organic room-temperature phosphorescence: toward high-efficiency ultralong emission *via* nonradiative channel constriction. *Adv. Funct. Mater.* **2026**, *36*, e17762.
42 Dai, W.; Li, G.; Zhang, Y.; Ren, Y.; Lei, Y.; Shi, J.; Tong, B.; Cai, Z.; Dong, Y. Controllable modulation of efficient phosphorescence through dynamic metal-ligand coordination for reversible anti-counterfeiting printing of thermal development. *Adv. Funct. Mater.* **2023**, *33*, 2210102.
43 Feng, R.; Wang, M.; Zhang, Z.; Hu, P.; Wu, Z.; Shi, G.; Xu, B.; Liu, H.; Ma, L. J. Polymer-based long-lived phosphorescence materials over a broad temperature based on coumarin derivatives as information anti-counterfeiting. *ACS Appl. Mater. Interfaces* **2023**, *15*, 30717–30726.
44 Jiang, N.; Li, G. F.; Zhang, B. H.; Zhu, D. X.; Su, Z. M.; Bryce, M. R. Aggregation-induced long-lived phosphorescence in nonconjugated polyurethane derivatives at 77 k. *Macromolecules* **2018**, *51*, 4178–4184.
45 Yao, Y.; Huang, D.; Han, P.; Peng, X.; He, X.; Xu, H.; Qin, A.; Tang, B. Z. Boric acid cross-linking strategy for enhancing room temperature phosphorescence of poly(vinyl alcohol)-doped films. *ACS Mater. Lett.* **2025**, *7*, 133–140.
46 Smith, G. J.; Dunford, C. L.; Roberts, P. B. The photostability and fluorescence of hydroxycoumarins in aprotic solvents. *J. Photochem. Photobiol. Chem.* **2010**, *210*, 31–35.
47 Dong, M.; Feng, H.; Gao, W.; Li, D.; Liang, F.; Wen, L.; Su, Z. Efficient triplet–triplet energy transfer that activates room-temperature phosphorescence of coumarin guests. *New J. Chem.* **2026**, *50*, 819–825.
48 Guo, Y.; Chen, K.; Hu, Z.; Lei, Y.; Liu, X.; Liu, M.; Cai, Z.; Xiao, J.; Wu, H.; Huang, X. Metal ions as the third component coordinate with the guest to stereoscopically enhance the phosphorescence properties of doped materials. *J. Phys. Chem. Lett.* **2022**, *13*, 7607–7617.
49 Piccolo, D.; Castro, J.; Rosa-Gastaldo, D.; Bortoluzzi, M. Luminescent manganese(ii) iminophosphorane derivatives. *Molecules* **2025**, *30*, 1319.
50 Zhang, K. Efficient energy transfer from organic triplet states to $Mn^{2+}$ dopants for dynamic tunable multicolor afterglow in 1D hybrid cadmium chloride. Chem. Sci. **2025**, *16*, 6104–6113.
51 Song, E.; Han, X.; Zhou, Y.; Wei, Y.; Jiang, X. F.; Ye, S.; Zhou, B.; Xia, Z.; Zhang, Q. Long-lived photon upconversion phosphorescence in $RbCaF_3$:$Mn^{2+}$, $Yb^{3+}$ and the dynamic color separation effect. *iScience* **2019**, *19*, 597–606.
52 Rodríguez, H. B.; San Román, E. Effect of concentration on the photophysics of dyes in light-scattering materials. *Photochem. Photobiol.* **2013**, *89*, 1273–1282.
53 Trang, T. T.; Pham, T. T. H.; Dang, N. V.; Nga, P. T.; Linh, M. V.; Vu, X. H. Revealing the high efficiency of fluorescence quenching of rhodamine B by triangular silver nanodisks due to the inner filter effect mechanism. *RSC Adv.* **2024**, *14*, 9538–9546.
54 Wang, Z.; Meijerink, A. Concentration quenching in upconversion nanocrystals. *J. Phys. Chem. C* **2018**, *122*, 26298–26306.